

Double-Diffusive effects in a Dam Break Experiment

Frédéric Laliberté

January 16, 2008

Abstract

A rotating dam break experiment was conducted with a vertical barrier at the midpoint separating a salt solution in one half of the channel and a sugar solution in the other half. Sugar diffuses slower than salt so that it plays a role equivalent to oceanic salt which diffuses slower than heat. In simpler experiments with fresh water in one half and a slightly denser saline solution in the other, a tongue of fresh water flows along the surface on the right side of the channel and the interface at the surface dividing the two fluids becomes unstable and sheds fresh vortices into the salt solution. When the less dense fluid contains salt and the heavier fluid contains sugar, with a small initial density difference, much weaker instabilities occur and vertical diffusion of salt into the sugar solution reduces the density of the saline solution and therefore increase the density differences. This local increase in reduced gravity, resulting in spatial variations of the deformation scale, widens the boundary current, suppresses the instabilities and enhance the rightward flux of mass.

1 Introduction

Previous works on gravity currents are numerous with early results dating as far back as Benjamin [1], who mentions even earlier work by von Kármán (1940). In his paper, Benjamin describes non-rotating gravity currents in a two-layer system and derives some of the first rigorous results, including an asymptotic expression for the velocity of propagation of a gravity current over a deep layer. This result, which assumes that away from the head of the current the depth attains a constant value H , states that the head's velocity should be $c = \sqrt{2g\frac{\Delta\rho}{\rho}H}$. This system has been extensively studied in the laboratory with results that vary depending on the flow regime. In most flows, viscosity as well as mixing tend to remove the factor $\sqrt{2}$, and other effects, such as the interaction with a wall perpendicular to the motion, tends to affect the velocity dramatically.

In a rotating environment, the dynamics may be expected to be quite different with the current being constrained to propagate along a wall due to Coriolis deflection [3]. However, apart from an initial adjustment, it has been shown by Stern, Whitehead and Hua [5] both theoretically and experimentally that the gravity current nose speed should be essentially the same as for the non-rotating case, with similar dependence on viscous, mixing and boundary interaction effects. In another set of experiments, Stern [4] investigated the evolution of a coastal gravity current and observed strong instabilities. These instabilities often develop filaments and smaller eddies, impacting on the entrainment (and detrainment) capabilities of the jet.

As described by Stern and Chassignet [2], several laboratory experiments in a rotating basin have been carried out in which a lighter fluid (fresh water) flows as a boundary current over a denser environment (salty water). In these experiments, detachment of eddies is common and is thought to reduce significantly the downstream transport of fresh water. The impact on the jet is observed to be important in comparison with the theoretical laminar flow with a large amount of detrainment occurring due to small scale eddies separating from the jet. Depending on the nature of these small scale turbulent features, the current can be observed to effectively widen or actually “eject” mass to its surroundings.

In double diffusive experiments, where one of the fluids is a sugar solution and the other is a salt solution, it has been observed [6] that these instabilities disappear, that the gravity current propagates faster and that the boundary current is wider. The exact mechanism on how the instabilities are damped was not clarified nor how this influences the effectiveness of the flow to transport lighter fluid over heavier fluid.

The goal of this report is to demonstrate, for the range of parameters investigated, that the flow is primarily driven by double diffusion and that it increases the transport of lighter fluid over heavier fluid. We also show that the rate at which the boundary current widens is higher in the regions where a non-diffusive current would shed eddies, leading us to propose that it is the local increase in the deformation radius by double diffusion that suppresses the interfacial instabilities. In section 2 we describe the experimental setup and in section 3 how we processed our photographic data. In section 4 we discuss our results, always comparing double-diffusive experiments with their non-diffusive counterparts. We finally conclude in section 5 and we propose a theoretical model in appendix A for future work.

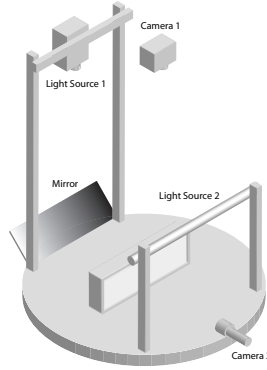


Figure 1: Our experimental setup, where camera 2 was not used. Taken from [6].

2 The Experiment

2.1 Experimental Setting

The experiment was conducted in a 60 cm \times 10 cm tank with a removable barrier in the middle. The tank was on a table rotating with angular velocity Ω where $f = 2\Omega = 1.25 \text{ s}^{-1}$. A co-rotating digital still camera was placed directly above the tank and a mirror inclined at 45° to the horizontal was used in order to obtain a side view. The lighter fluid, placed on the left, was dyed blue and we used approximately 1 liter of each fluid, leading to a depth of $\approx 3.3 \text{ cm}$. The experiments were carried through in two distinct sessions, one during the summer of 2007 and the other during the month of October 2007. The setup changed slightly between these two sessions, with the major difference being the introduction of a motor to lift the gate. The motor has the advantage of lifting slowly enough that only limited turbulence is produced by the removal of the gate but with the drawback that it takes several rotations before the gate is lifted, thus impacting on the initial evolution of the flow. The experimental schematics are depicted in figure 1.

2.2 Experimental Parameters

The environment was maintained at a constant temperature, 20°C , and the atmospheric pressure was assumed to be constant. The rotation frequency was kept constant at a value of $f = 1.25 \text{ s}^{-1}$. This choice was to some extent arbitrary and was mainly dictated by experimental manipulations. A faster rotation would have made manipulations more intricate without having a profound impact on the physics of the experiment. This frequency, corresponding to a rotation period of 10.25 s, was conveniently in phase with our digital camera's highest shooting rate, at 11 s. This

Table 1: Experimental parameters and the number of experiments conducted

$\Delta\rho$ (g cm ⁻³) \backslash ρ_0 (g cm ⁻³)	0.99823	1.0100	1.0400
2.0×10^{-4}	1	1	1
3.5×10^{-4}	1	1	1
5.0×10^{-4}	1	1	1

(a) Summer 2007

$\Delta\rho$ (g cm ⁻³) \backslash ρ_0 (g cm ⁻³)	0.99823	1.0050	1.0100	1.0150
0.8×10^{-4}	2	3	3	3
2.0×10^{-4}	3	3	3	4
3.5×10^{-4}	3	3	3	3

(b) October 2007

The experiments with $\rho_0 = 0.99823$ g cm³ were carried with fresh water on top and salty water on the bottom so that in these situations $\Delta\rho = \rho_T - \rho_f$. For all other experiments, the salty solution was on top and $\Delta\rho = \rho_S - \rho_T$.

slight out-of-phase leads to a slow phase change, reducing possible biases due to position.

In order to describe our experiments, we use two parameters, $\Delta\rho = \rho_S - \rho_T$ and $\rho_0 = \rho_S$, where ρ_S and ρ_T are the density of sweet water and salty water, respectively. The first quantity indicates how fast the boundary current should propagate initially ($v_i \approx \sqrt{g(\Delta\rho/\rho_0)H}$) whereas the second quantity is a measure of how strong double diffusion is at the removal of the gate (the diffusive fluxes are proportional to $\rho_0 - \rho_f$, where ρ_f is the density of fresh water). Note that the sign of $\Delta\rho$ indicates which of the two layers is salty. These parameters have been investigated for the values shown in table 1.

Negative values of $\Delta\rho$ for $\rho_0 > \rho_f = 0.99823$ g cm³ would lead to “sugar fingers”, the salty-sweet system’s counterpart of salt fingers in the warm-salty system, a situation we decided not to study because of its complicated layer structure.

3 Data Acquisition

The fluid in each experiment was calibrated with a 10^{-5} g cm $^{-3}$ accurate densiometer. These values were assumed highly accurate with inconsequential associated errors since we were computing density differences of the order of 10^{-4} g cm 3 . The rest of the data was acquired by two cameras, both top mounted with a side view provided by a 45° mirror. One of the cameras was a low-resolution analog camera, used mainly as a quick experiment assessment tool. The second camera, a still 10 megapixels digital camera (resolution of 2448×3264 pixels), was our reliable data acquisition apparatus. The camera was set to take a shot every 11 seconds (the shortest interval allowed by the equipment) with constant lighting and fixed exposure settings. The result is a sequence of high resolution photos. The main uncertainty remaining is the exact moment that the gate was pulled. This exact moment is in fact immaterial to our analysis since we will look mainly at time derivatives of quantities and never compare two quantities at a fixed time after the removal of the gate.

3.1 Image Processing

The image files produced by the camera, once loaded in Matlab, have three components for each pixel: one red, one green and one blue. If blue dye was used, one can infer the thickness of the blue layer by the intensity of blue color, after having removed the constant signal coming from shadows and other constant variations in spatial light intensity. In figure 2, we show a photo that includes the side view. For $y > 0$, we see the fluid from directly above and for $y < 0$, we see the side view through the 45° mirror. This means that one can recover the z -coordinates by simply writing $z = -y$ for $y < 0$. In the figure, the side view shows a linearly decreasing depth in x from 10 cm to 20 cm to the right of the barrier (located at $x = 0$ in the graph). Since during the experiment we could easily assess that the most blue dye was located at $y = 0$ cm, we know that along this line the thickness decreases linearly.

Next, we show in figure 3 the adjusted color intensity for the three color components along the line $y = 0$ in the photo. The adjustment refers to the removal of white noise from the blue color, by using the empty tank as a reference point. In this figure, we see clearly that the intensity increases linearly (the line is a linear fit) over the same region over which the thickness decreases linearly. From this, we concluded that there is a linear correspondence between thickness and adjusted blue color intensity. This linear relation is computed independently for each experiment, in order to remove systematic errors.

One of the remaining problems is to filter out the noise when the intensity of

blue color reaches saturation. Even though the intensity is on average constant in the no-dye region, the fluctuations can be quite large, hence a need to filter out this unnecessary noise. If one would simply demand that negative thicknesses be ignored, important noise would be left. Instead, we realized that the red color intensity was almost a step function at the nose (as can easily be seen from figures 2 and 3), and so we used the red component as a simple cutoff criterion (we cut off at > 70 of intensity) to decide when the thickness was zero, regardless of the noise.

One could inquire why the green component of the image was not used instead of the blue. After all, in figure 3 the green intensity and the blue intensity seem to behave similarly. However, there is one major difference: the green color is everywhere less intense, making our thickness inference more susceptible to noise for thick regions, leading to a less accurate layer thickness analysis.

In the remaining part of this report, when we refer to the thickness we refer to the linearly inferred thickness plus the red-color filtering that we just discussed.

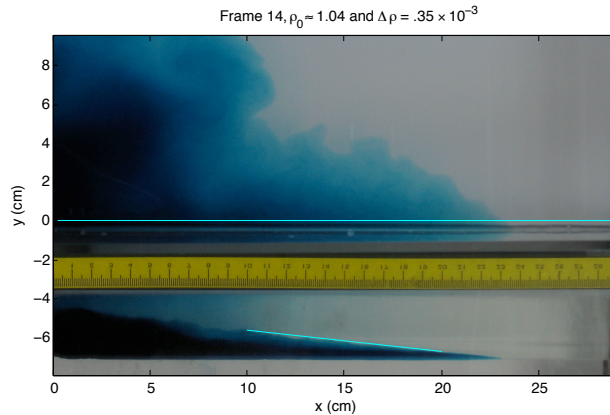


Figure 2: Picture taken during an experiment. In the upper part of the picture, the line shows the section along which figure 3 is plotting the color intensities. In the lower part, the line is there to show how linear the depth is in this region.

4 Results

4.1 Evolution of the jet

Non-Diffusive case, fresh water over salty water In the non-diffusive case, the jet starts off as a laminar boundary current of width determined by the radius

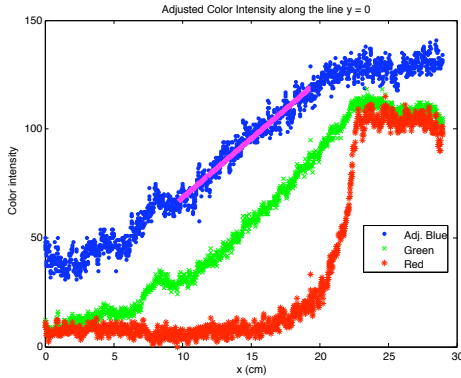


Figure 3: The color intensity along the line in figure 2. The line is a linear fit on the blue color. Note the sudden increase in red color at $x \approx 22$ cm in the transition zone between blue dye and no dye.

of deformation [4] and is usually accompanied by an unstable interface that fluxes mass toward the center of the tank. Sometimes eddies are formed (for small density differences) and detach themselves from the right-flowing current.

In figure 4, we show the time-evolution of a non-diffusive dam break experiment. What is observed is typical of small reduced gravity experiments, with strong instabilities and numerous eddies. Note how most of the dye is restricted to a region close to the boundary, with the transition zone between this current and the interior flow being almost entirely populated with instabilities and their generated eddies. The evolution is constant with the first onset of instabilities appearing very shortly after the removal of the gate. Otherwise, most of the dye seems to be transported first by the boundary jet with a secondary transport towards the interior, by the deformation of the interface. Notice in figure 4 the big lump of blue dye that seems to be trapped left of $x = 5$ cm; this feature was observed systematically in all non-diffusive experiments.

Double Diffusive case, salty water over sweet water The double diffusive case has been extensively studied in non-rotating environments. The typical double diffusive jet evolution with rotation has not often been described and it still remains unclear how the instabilities observed in the non-diffusive case are suppressed.

In figure 5, we show the evolution of the jet for one of the double diffusive experiments with $\Delta\rho$ about the same as that in figure 4. One quickly notices that the boundary current is wider and has progressed farther than the one in figure 4. It is also relatively shallow away from the boundary. What is striking about these

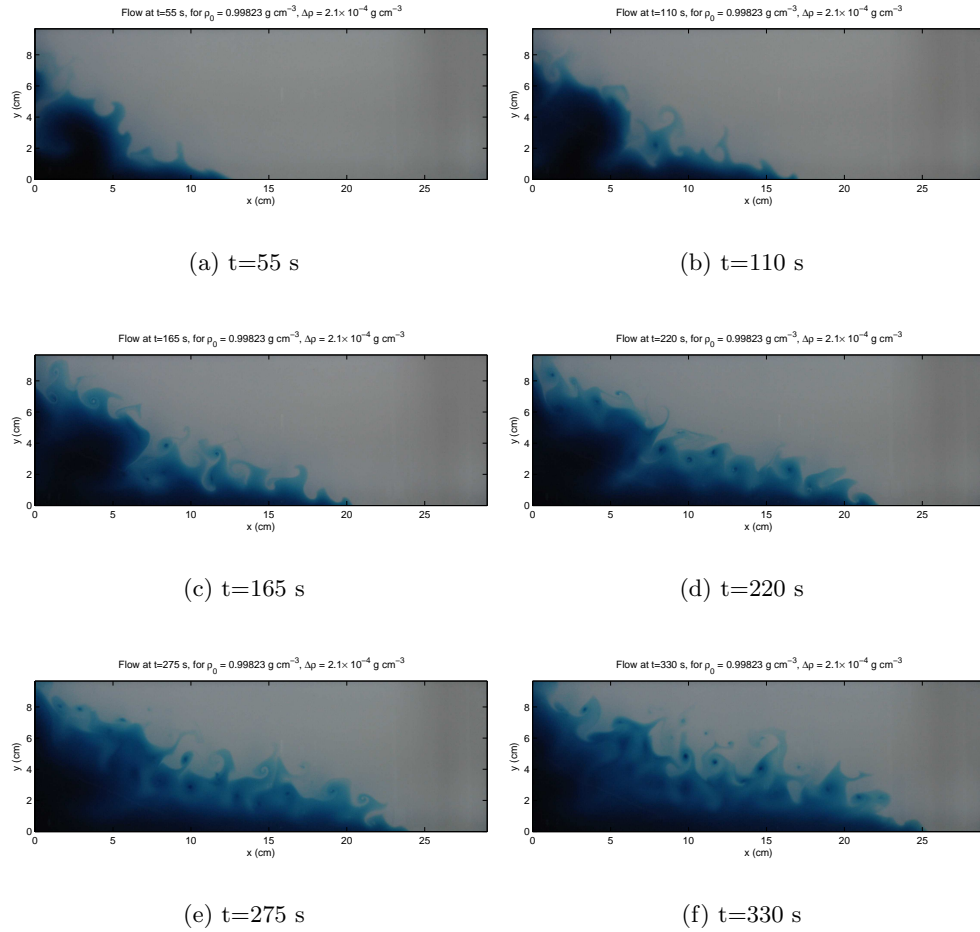


Figure 4: Time evolution of a non-diffusive front for $\rho_0 = 0.99823 \text{ g cm}^{-3}$ and $\Delta\rho = 2.1 \times 10^{-4} \text{ g cm}^{-3}$.

experiments is how they inhibit the development of the instabilities. One can see in figure 5(d), the interface growing filaments, in precisely the same manner as for the non-diffusive jet. However, for some reason, these are not sustainable in a double-diffusive environment and collapse soon after their first appearance. They usually simply evolve as to reform another interface, a bit further from the boundary.

Referring again to figure 5, one sees how a large part of the blue dye actually does not have to propagate first through the boundary current but instead is able to penetrate much further. This is in stark contrast with the non-diffusive experiment where most of the dye was confined to $x < 5$ cm or to the boundary current. In the double diffusive case, the bulk of the blue dye does not even seem to be confined, except that the interior circulation appears to be slower than the propagation speed of the jet. This gives a second way for double-diffusive experiments to flux mass rightward, a statement that will be clarified later.

4.2 Nose Displacement

The speed at which the tip of the gravity current propagates is directly affected by the gravitational forcing associated to $\Delta\rho$. This means that any change in $\Delta\rho$, through diffusion for example, will influence the speed at which the nose moves. In order to quantify how much, we computed the nose position as a function of time for each experiment. Then, we found the linear fit of the nose position over the time interval $[t_{15}, t_{25}]$, where the time t_{x_0} is the first time when the nose reaches x_0 . The slope of the linear fit gives the nose speed over that interval. We have plotted these speeds as a function of ρ_0 in figure 6.

For the two smaller $\Delta\rho$, we observe a clear tendency of the flow to be accelerated with increasing ρ_0 but for the largest $\Delta\rho$, this tendency seems absent. One explanation is that as $\Delta\rho$ increases the initial velocity increases, which reduces the time scale, but for fixed ρ_0 , the diffusive fluxes are kept constant. The compounded effect of diffusion over the course of an experiment will then be of the order of the time scale multiplied by the diffusive fluxes. Therefore, a smaller time-scale should lead to weaker total diffusive effects. One could imagine in the limit of very large $\Delta\rho$, for a fixed ρ_0 , to observe no clear effects of double diffusion before the nose reaches the end of the tank. In figure 7, we plotted the relative gain of speed by double diffusion for each $\Delta\rho$. The bigger the $\Delta\rho$, the smaller the relative gain is, which justifies our explanation.

Alternatively, one could argue that the error bars being as large as they are, these results should be taken with some reserve. This is clearly true for the largest $\Delta\rho$ but not for the smallest. More experiments would be needed to solve this problem, ideally with a longer tank for higher $\Delta\rho$.

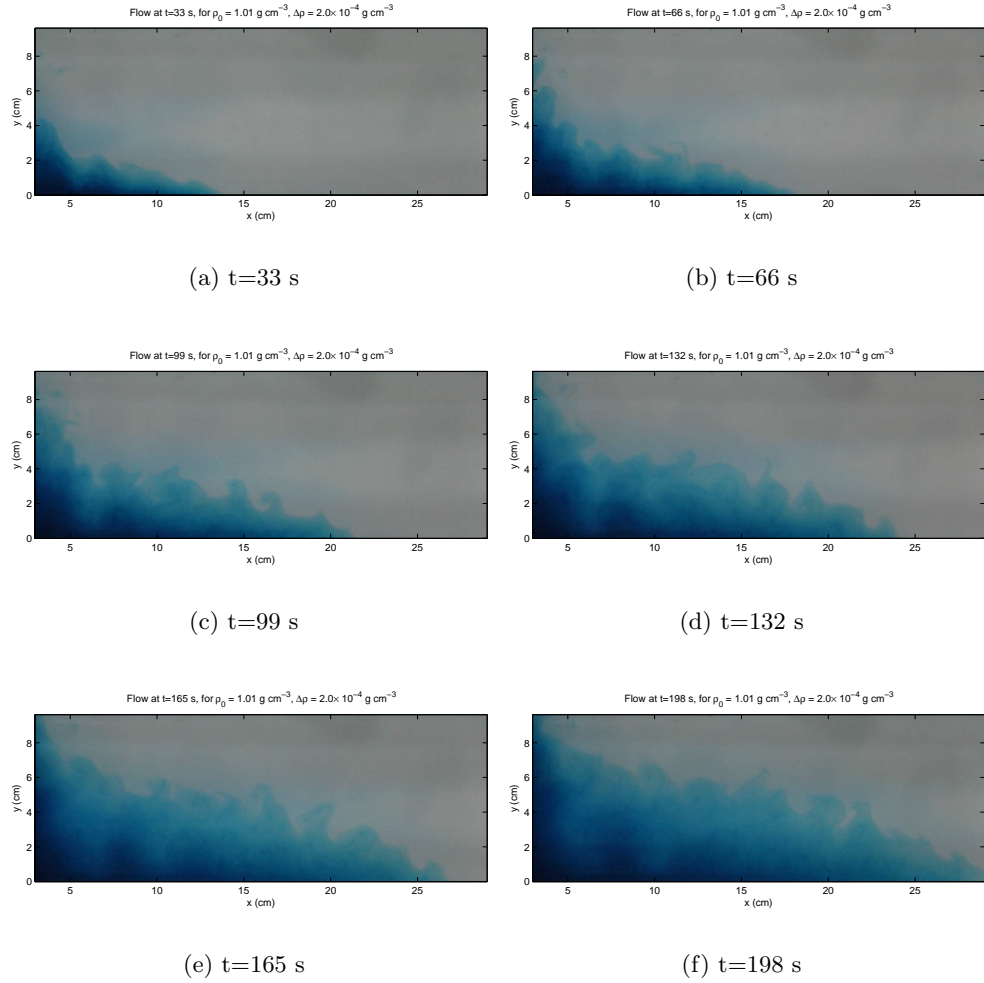


Figure 5: Time evolution of a double diffusive front for $\rho_0 = 1.01 \text{ g cm}^{-3}$ and $\Delta\rho = 2.0 \times 10^{-4} \text{ g cm}^{-3}$. Note that panel 5(f) occurs at a time between panels 4(c) and 4(d)

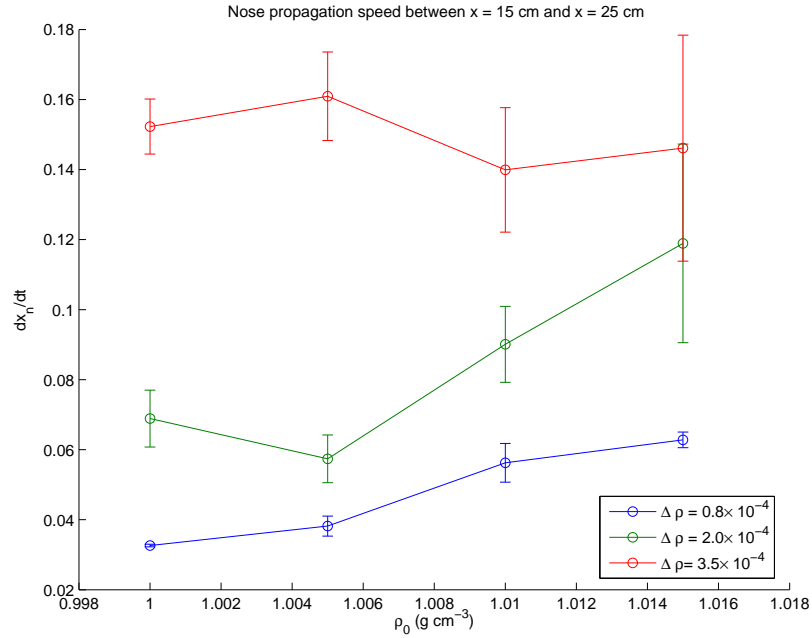


Figure 6: The linear fit velocity of the nose during its residence between $x = 15$ cm and $x = 25$ cm. Observe the dependence on ρ_0 for the two lower $\Delta\rho$ but no obvious dependence for $\Delta\rho = 3.5 \times 10^{-4} \text{ g cm}^{-3}$. The error bars are sampling standard deviations.

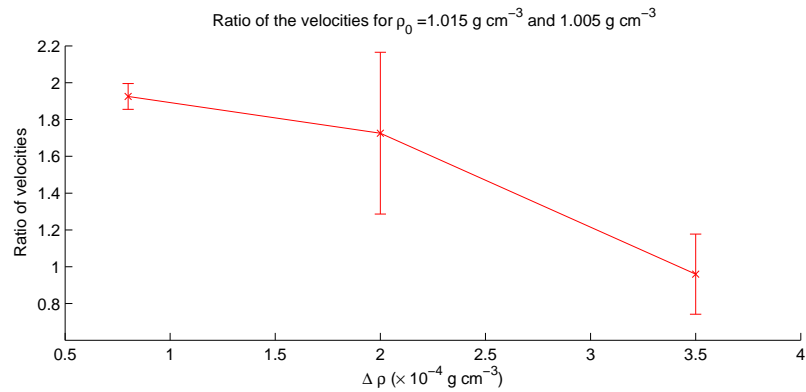


Figure 7: The ratio of the nose speed for $\rho_0 = 1.015 \text{ g cm}^{-3}$ to the velocity for $\rho_0 = 1.005 \text{ g cm}^{-3}$. Observe the decrease in ratio with increasing $\Delta\rho$.

4.3 Mass transport

The nose speed is an important quantity because it gives us an idea of how fast the system is able to transport lighter fluid to the right. It is however limited in scope because it only tells us how fast the current close to the wall at $y = 0$ cm is going. In the situation where the bulk of the mass is transported close to the wall, this velocity multiplied by the cross-section of the boundary current would be equivalent to the mass transport. But if that is not the case and an important part of the transport is located far from the wall, this velocity does not give the whole picture. One could imagine a fast boundary current that releases an important quantity of slow moving fluid towards the interior. The effect would be a fast nose and a wide current that would not flux much more mass than a slower current that does not eject any mass towards increasing y . The mass transport thus appears to be an important feature of the flow worth investigating.

In order to compute the mass transport, we assume that the blue dye is a tracer and that each layer is shallow enough that it has a velocity uniform in z :

$$\partial_t h + \nabla \cdot (h\mathbf{u}) = 0 \quad (1)$$

where h is the thickness of the blue layer.

Since there is no flow normal to the side walls, if we integrate over the region to the right of a vertical line x , we get

$$\partial_t \left[\int_x^{30} \int_0^{10} h \, dx \, dy \right] = \int_0^{10} h(x, y) u(x, y) \, dy \quad (2)$$

where the term in the time derivative corresponds to the total amount of dye at the right of x , that will be denoted $\mathcal{H}(x, t)$, and where the right hand side corresponds to the total horizontal dye flux across the vertical line at x , that will be denoted $\mathcal{F}_h(x, t)$.

This means that from our data we can recover the horizontal flux through any vertical line. This can be done by fixing an x , $x = 15$ cm for example, computing $\mathcal{H}(15, t)$ for all time and then taking the time derivative. This way, we can observe how efficient our currents are at transporting mass rightward. Using the same approach as with the nose speed, we compute the derivative of $\mathcal{H}(15, t)$ by using a linear fit on the time interval when the nose is between $x = 25$ cm and $x = 30$ cm. We are using a different interval because as the nose crosses the line $x = 15$ cm, $\mathcal{H}(15, t)$ increases non-linearly until the nose is sufficiently far.

In figure 8, we plotted the fluxes at 15 cm as a function of ρ_0 . The flux is seen to increase with ρ_0 but it is unclear why there so much variability. Clearly, higher density differences are leading to apparently smaller gains, which is coherent with our discussion about velocities.

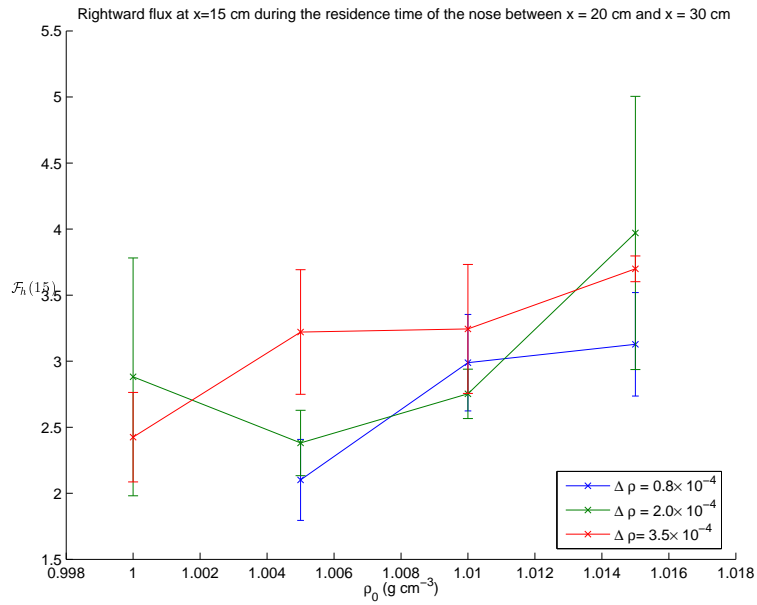


Figure 8: Flux at $x = 15$ cm. Generally the flux increases with ρ_0 except for $\rho_0 = 0.99823$ g cm $^{-3}$ and $\Delta\rho = 2.0 \times 10^{-4}$ g cm $^{-3}$. Considering the high level of uncertainty associated with this point, we attribute this to statistical errors. The absence of data for the non-diffusive experiment with the lowest $\Delta\rho$ is due to the fact that the current did not propagate far enough in the tank.

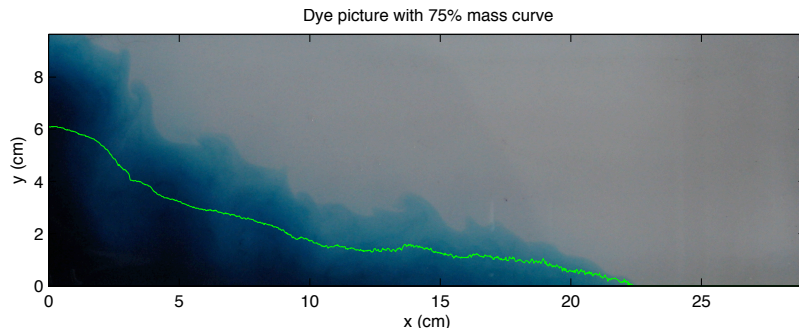


Figure 9: An example of the curve $y_{.75}(x)$ for a double diffusive experiment. For each x , $y = y_{.75}(x)$ corresponds to the point below which lies 75% of the mass on the vertical passing by x .

4.4 Area Increase

Another striking feature of double diffusive gravity currents is how their width exceed that of non-diffusive currents. In order to get a measure of the width, we first tracked the evolution of the interface by using an uncommon technique. The technique uses the $h(x, y, t)$, the depth in space and time, and the function

$$y_p(x, t), \quad \text{such that} \quad \int_0^{y_p(x, t)} h(x, y', t) dy' = p \int_0^{10} h(x, y', t) dy', \quad (3)$$

where we must have $p \leq 1$.

If one sets $p = 1$, $y_1(x, t)$ is simply the interface between the blue and the transparent fluid. By using $p < 1$, $y_p(x, t)$ is the curve below which lies a fraction p of the mass on the vertical line passing through x . It enables us to track the interface without really tracking it, thus reducing the noise, especially in non-diffusive experiments. Also, it emphasizes the fact that even though the interface has important physical properties, it is what happens to the *bulk* of the flow that interests us. We show an example of such a curve with $p = 0.75$ in figure 9.

Now, one can compute the area $A_p(t) = \int_0^{30} y_p(x, t) dx$, thus finding the area occupied by the fraction p of the mass closest to the boundary at $y = 0$ cm. Using this technique on our data, we realized that on the time interval where the nose lies between $x = 15$ cm and $x = 25$ cm, $A_p(t)$ is almost a linear function of time. Computing a linear fit on this function over that time interval is thus justified and the slope of the fit is then a good approximation of the time derivative $\frac{dA_p(t)}{dt}$. This quantity is then giving us an idea how fast the bulk of the fluid is spreading.

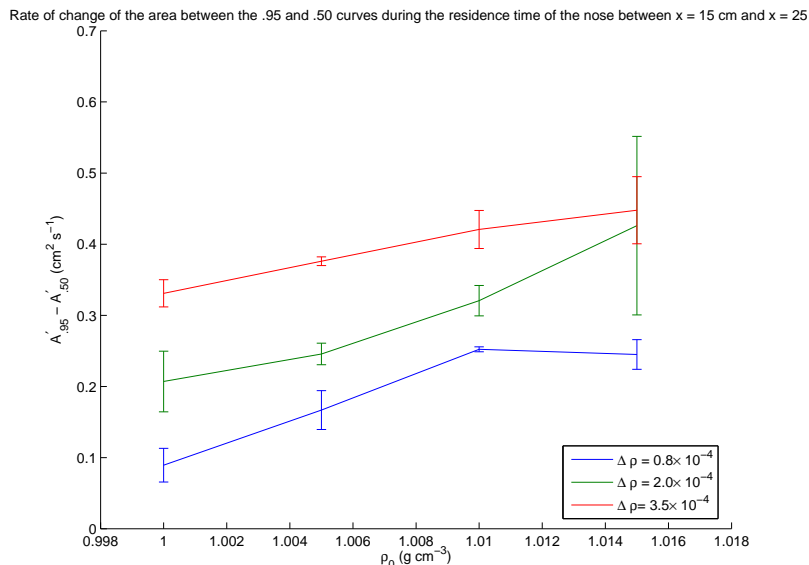


Figure 10: The linear fit rate of change of $\frac{dA_{.95}}{dt} - \frac{dA_{.5}}{dt}$ during the residence time of the nose between $x = 15$ cm and $x = 25$ cm. Observe a clear increase in the rate of change of the area for increasing ρ_0 . Only the experiments with $\rho_0 = 1.015$ g cm $^{-3}$ have higher uncertainties but not enough to make the previously mentioned tendency be questionable. The error bars are sampling standard deviations.

Dilatation of the interior flow. The flow can be qualitatively split into two regions: the boundary current and the interior flow. The boundary current contains most of the mass, is concentrated close to the wall at $y = 0$ cm and its dynamic is to first order characterized by the nose velocity. The interior flows is defined as the slow moving, shallow and instabilities prone region that remains. When one is evaluating how the bulk of the flow is spreading using the previously described technique, both the evolution of the boundary current and of the interior flow contribute to the analysis. Since the two regions have qualitatively different dynamics, we should not expect to capture any feature particular to any one of these regions. We will therefore have to devise an analysis that enables us to observe each region separately.

In order to do so, we need to have a quantitative definition of each region. Any such definition will be to some extent arbitrary so here we decide to define the interior flow as the region that has 50% of the mass furthest from the boundary. Basically, it is the region contained between the curve $y_{.5}(x, t)$ and $y_{.95}(x, t)$. The rate of change of its area, $\frac{dA_{.95}}{dt} - \frac{dA_{.5}}{dt}$, indicates how the bulk of the interior spreads. The results are shown in figure 10.

It shows a clear increase in area with ρ_0 , implying a general increase in defor-

mation radius. One could compute the average widening, or the average increase in deformation radius, by dividing the rate of change by 20 cm, the average length of the boundary current when the derivative was taken. This would be a way to quantify the bulk diffusion but what interests us is where most of this diffusion occurs, not how much it occurs on average. To accomplish this, we have to develop another special technique.

Spatial distribution of area increase. We start by subdividing the interval $[0, x_N(t)]$, where $x_N(t)$ is the nose position, in n subintervals $[x_i, x_{i+1}]$. Then we define the area under the curve $y_p(x, t)$ in the i^{th} subinterval by

$$a_p^{(i)}(t) = \int_{x_i}^{x_{i+1}} y_p(x, t) dx. \quad (4)$$

Summing up and taking the time derivative,

$$\frac{dA_p}{dt} = \sum_{i=1}^N \frac{da_p^{(i)}}{dt} \quad (5)$$

where A_p is as defined in section 4.4.

The functions $\frac{da_p^{(i)}}{dt}$, the rates of change of the area in the i^{th} subinterval, are the quantities we would like to recover because they locally quantify how fast the flow spreads towards the interior. But what we have now is one equation for n unknowns, which is highly underdetermined. Thus, in order to make any progress, we have to make some assumptions. We assume that for any p_1, p_2 such that $.95 \geq p_2 > p_1 \geq .5$ we can write

$$\frac{da_{p_2}^{(i)}}{dt} - \frac{da_{p_1}^{(i)}}{dt} = \bar{a}'_i \left(\frac{a_{p_2}^{(i)}(t) - a_{p_1}^{(i)}(t)}{a_{.95}^{(i)}(t) - a_{.5}^{(i)}(t)} \right), \quad (6)$$

which means that every subinterval has an uniform rate of area increase \bar{a}'_i . The factor is the fraction of the area between y_{p_2} and y_{p_1} with the total area of the interior flow in the i^{th} subinterval.

We then divide the interval $[.5, .95]$ in m subintervals $[p_j, p_{j+1}]$, yielding a system of m equations for \bar{a}'_i ,

$$\frac{dA_{p_{j+1}}}{dt} - \frac{dA_{p_j}}{dt} = \sum_{i=1}^n \bar{a}'_i(t) \left(\frac{a_{p_{j+1}}^{(i)}(t) - a_{p_j}^{(i)}(t)}{a_{.95}^{(i)}(t) - a_{.5}^{(i)}(t)} \right), \quad (7)$$

which is of the form $M\xi = b$ with the columns of M summing to 1.

If $m = n$, this system has a unique solution. However, this solution will most likely result in negatives \bar{a}'_i , which would indicate a reduction of area in some interval

$[x_i, x_{i+1}]$. Even if such a situation could be physically justified, we would like to avoid it for numerical stability purposes. So, instead, we solve the system in a least-squares sense demanding that the solution be everywhere positive and that the total change in area be conserved,

$$\frac{dA_{.95}}{dt} - \frac{dA_{.5}}{dt} = \sum_{i=1}^n \bar{a}'_i(t). \quad (8)$$

This is an optimization problem that depends on the initial guess, here chosen as a random vector, to reduce bias.

We can then convert the \bar{a}'_i to local width increase by

$$\bar{l}'(x, t) = \bar{a}'_i \left(\frac{y_{.95}(x, t) - y_{.5}(x, t)}{a_{.95}^{(i)}(t) - a_{.5}^{(i)}(t)} \right), \quad \text{for } x \in [x_i, x_{i+1}]. \quad (9)$$

Since by construction $\bar{l}'(x, t) \geq 0$, it can be transformed into a distribution and one can compute its moments. For example, one can compute $\bar{x} = \langle x_N - x \rangle_{\bar{l}'}$, its first moment with respect to the nose position. This value tells us where the average widening takes place. If it is close to 0, it means most of the widening happens at the nose whereas, if it is non-zero, the widening occurs on average at \bar{x} cm at the left of the nose. In figure 11, we show the results for our experiments. We observe that for non-diffusive experiments, the increase is close to the nose, which is not surprising considering that our technique does not correct for the increase in area due to the gravitational propagation of the boundary current. For diffusive experiments, however, most of the widening occurs away from the nose, at about 5 cm to the left, precisely where the unstable eddies would form in the non-diffusive case.

5 Conclusion

The double diffusive rotating dam break experiment shows significant qualitative differences from the non-diffusive one, with most instabilities suppressed. The resulting boundary currents are wider and transport mass more effectively. From our data, we are able to extract a clear trend that shows an increase in nose velocity with increasing ρ_0 , mainly for smaller $\Delta\rho$. Moreover, our data suggest that the rightward flux of mass is enhanced with increasing values of ρ_0 . This indicates that double diffusive systems should be more efficient at transporting mass than non-diffusive ones, with the effect of ρ_0 dominating that due to $\Delta\rho$ in diffusive experiments.

This means that over the course of the experiment, $\Delta\rho$ must acquire a significant spatial variation, in order to drive the system. Such a spatial variation, one can hypothesize, must increase the local radius of deformation, thereby widening

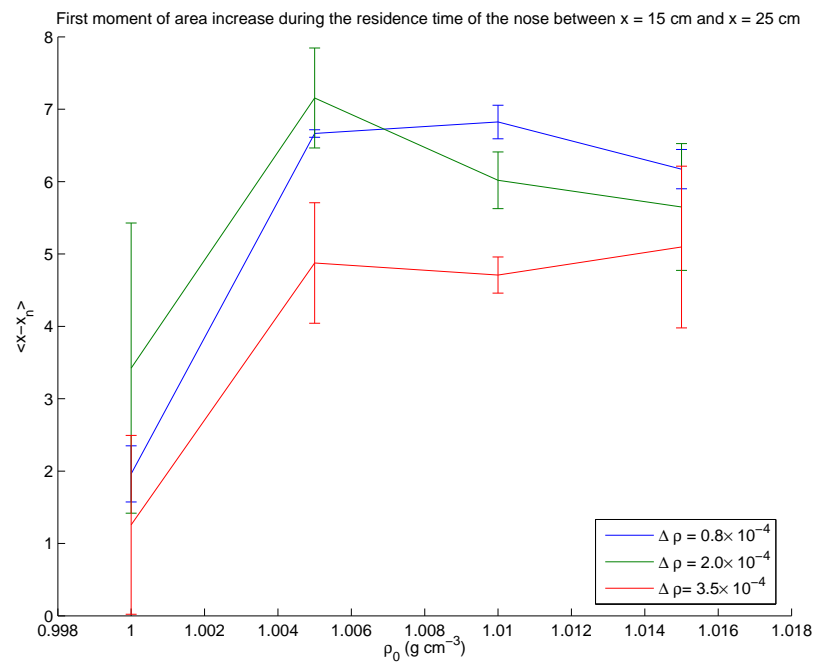


Figure 11: The average distance from the nose where the widening of the jet occurs. Note how much closer to the nose the non-diffusive experiments widen. The error bars are sampling standard deviations.

the boundary current. Variations of radii of deformation should also influence the turbulent cascade and, hence, the energy spectrum distribution of the system since it is the scale at which eddies evolve. This means that major spatial variations in deformation scale would most likely distort and make unsustainable two-dimensional type turbulent eddies.

We have demonstrated that the width of the boundary current in diffusive experiments exceeds that in non-diffusive ones, and that the width increases with increasing values of ρ_0 . In diffusive experiments, the first moment of this widening was shown to occur in the region where the turbulent eddies form in non-diffusive experiments. In contrast, in non-diffusive experiments it occurred close to the nose, which is consistent with the biases of our measurement method. This strongly suggests that the deformation radius in regions where instabilities would normally develop in non-diffusive experiments increases in double diffusive experiments. This leads us to conclude that this local inflation of the deformation radius destroys the instabilities.

This conclusion remains to be investigated using more theoretical models. In appendix A, we propose a simple toy model that could verify this explanation. It is based on a two-layer QG model with spatially varying radius of deformation. We expect that in such a model growth of instabilities will be slowed, if not removed, and that the width of the boundary current will be wider than in situations with a constant radius of deformation.

6 Acknowledgments

The success of this project must be entirely credited to George Veronis' enthusiasm and enlightening physical insights. Without the numerous hours spent in the lab debating about science and being amazed by the beautiful vortices created in our experiments this project would never have attained the same maturity. I am also grateful to Keith Bradley and his dedication at making things work. Finally, I would like to thank WHOI for this beautiful opportunity as well as Claudia Cenedese and Jack Whitehead for organizing such a memorable summer.

A Two-layer QG with non-uniform densities

To derive the shallow water equations for non-uniform densities, one makes the momentum budget in a test volume containing a whole layer:

$$\begin{aligned}
\partial_t \rho_1 h_1 + \nabla \cdot (\rho_1 h_1 \mathbf{u}_1) &= 0, \\
\partial_t (\rho_1 h_1 \mathbf{u}_1) + \nabla \cdot (\rho_1 h_1 \mathbf{u}_1 \otimes \mathbf{u}_1) + \mathbf{f} \times \rho_1 h_1 \mathbf{u}_1 &= -g \nabla (\rho_1 \frac{h_1^2}{2}) - g \rho_1 h_1 \nabla h_2, \\
\partial_t \rho_2 h_2 + \nabla \cdot (\rho_2 h_2 \mathbf{u}_2) &= 0, \\
\partial_t (\rho_2 h_2 \mathbf{u}_2) + \nabla \cdot (\rho_2 h_2 \mathbf{u}_2 \otimes \mathbf{u}_2) + \mathbf{f} \times \rho_2 h_2 \mathbf{u}_2 &= -g \nabla (\rho_1 h_1 h_2 + \rho_2 \frac{h_2^2}{2}) + g \rho_1 h_1 \nabla h_2,
\end{aligned} \tag{10}$$

These equations characterize the system if ρ_i are constants. However, here we want to allow them to vary in both space and time. We assume that $\rho_i = \rho_0 + \rho_T i + \rho_S i$ where ρ_0 is the density of pure water at some fixed temperature. ρ_T and ρ_S are the densities of salt and sugar respectively.

We assume that the two layers don't mix but that they can exchange chemicals. This leads to

$$\begin{aligned}
\partial_t (\rho_{\alpha i} h_i) + \nabla \cdot (\rho_{\alpha i} h_i \mathbf{u}_i) &= (-1)^i S_\alpha + D_{\alpha i}, \\
\partial_t \rho_0 h_i + \nabla \cdot (\rho_0 h_i \mathbf{u}_i) &= 0.
\end{aligned} \tag{11}$$

where the last expression implies conservation of volume since ρ_0 is constant.

S_α is the exchange of mass between the two layers. A heuristic candidate would be:

$$S_\alpha = \kappa_\alpha \rho_i (m_{\alpha 1} - m_{\alpha 2}) \sqrt{|\nabla h_2|^2 + 1} |\rho_{\alpha 1} - \rho_{\alpha 2}| \tag{12}$$

where $m_{\alpha i} = \frac{\rho_{\alpha i}}{\rho_i}$ is the mass fraction and κ_α is a diffusivity constant.

From these equations, one can find advection equations:

$$\frac{Dm_{\alpha i}}{Dt} = (-1)^i \frac{S_\alpha}{\rho_i h_i} + \frac{D_{\alpha i}}{\rho_i h_i} \tag{13}$$

Where the diffusion can be written as

$$\frac{D_{\alpha i}}{\rho_i h_i} = \bar{\kappa}_\alpha \nabla^2 m_{\alpha i}$$

or as any other mass-ratio diffusion.

From now on, we will drop the diffusion as it only add uninteresting complexity.

Equations After some manipulations, one gets the following equations:

$$\begin{aligned}
\partial_t h_i + \nabla \cdot (h_i \mathbf{u}_i) &= 0, \\
\frac{Dm_{\alpha i}}{Dt} &= (-1)^i \frac{S_\alpha}{\rho_i h_i}, \\
\gamma_i &= \frac{1}{\rho_i h_i} = \frac{1 - m_{Ti} - m_{Si}}{\rho_0 h_i}, \\
\frac{D\mathbf{u}_1}{Dt} + f \times \mathbf{u}_1 &= \mathbf{u}_1 \gamma_1 (S_T + S_S) - g \gamma_1 \nabla (\rho_1 \frac{h_1^2}{2}) - g \nabla h_2, \\
\frac{D\mathbf{u}_2}{Dt} + f \times \mathbf{u}_2 &= -\mathbf{u}_2 \gamma_2 (S_T + S_S) - g \gamma_2 \nabla (\rho_1 h_1 h_2 + \rho_2 \frac{h_2^2}{2}) + g \frac{\gamma_2}{\gamma_1} \nabla h_2.
\end{aligned} \tag{14}$$

March towards a QG formulation In order to find a QG formulation of the problem, one must first find the geostrophic winds. First, we assume a small Rossby number, leading to:

$$\begin{aligned}
f \times \mathbf{u}_1 &= \mathbf{u}_1 \gamma_1 (S_T + S_S) - g \nabla (h_1 + h_2) - g \frac{h_1}{2} \frac{\nabla \rho_1}{\rho_1}, \\
f \times \mathbf{u}_2 &= -\mathbf{u}_2 \gamma_2 (S_T + S_S) + g \frac{\rho_2 - \rho_1}{\rho_2} \nabla h_1 - g \nabla (h_1 + h_2) \\
&\quad - g (h_1 \frac{\nabla \rho_1}{\rho_2} + \frac{h_2}{2} \frac{\nabla \rho_2}{\rho_2}).
\end{aligned} \tag{15}$$

We now assume the density variations in horizontal to be small and that the mass exchange between the layers is relatively weak. This leads to the following streamfunctions:

$$\begin{aligned}
\psi_1 &= \frac{g}{f} (h_1 + h_2), \\
\nabla^2 (\psi_2 - \psi_1) &= -\nabla \cdot (\frac{g'}{f} \nabla h_1).
\end{aligned} \tag{16}$$

Advection of reduced gravity We now assume that the density difference is small between the two layers, so that $\rho_1 \approx \rho_2 = \bar{\rho}$. Subtracting the two advection equations, yields

$$\frac{D(\Delta m_\alpha)}{Dt} = \frac{S_\alpha}{\bar{\rho}} \left(\frac{1}{h_1} + \frac{1}{h_2} \right)$$

and adding the two diffusers,

$$\frac{D\Delta m}{Dt} = \frac{S_T + S_S}{\bar{\rho}} \left(\frac{1}{h_1} + \frac{1}{h_2} \right)$$

where $\Delta m = (m_{T2} + m_{S2}) - (m_{T1} + m_{S1})$.

Now, one can write

$$\frac{1}{\bar{\rho}}(S_T + S_S) = \sqrt{|\nabla h_2|^2 + 1}(\kappa_T \Delta m_T |\Delta m_T| + \kappa_S \Delta m_S |\Delta m_S|)$$

where we wrote $m_{\alpha i} \approx \frac{\rho_{\alpha i}}{\bar{\rho}}$.

Now, assuming $\frac{\kappa_S}{\kappa_T} \ll 1$, we obtain

$$\frac{D\Delta m}{Dt} \approx \kappa_T \Delta m_T |\Delta m_T| \left(\frac{1}{h_1} + \frac{1}{h_2} \right) \sqrt{|\nabla h_2|^2 + 1} \quad (17)$$

which can be seen as a equation of reduced gravity since $g' \approx g\Delta m$.

PV advections By defining the PVs:

$$q_i = \frac{\omega_i + f}{\rho_i h_i}$$

One get the following advection equations:

$$\begin{aligned} \frac{Dq_1}{Dt} &= -\gamma_1^2 f(S_T + S_S) + \gamma_1 J(\psi_1, \gamma_1(S_T + S_S)) - \frac{g}{2} J(\gamma_1, h_1), \\ \frac{Dq_2}{Dt} &= \gamma_2^2 f(S_T + S_S) + \gamma_2 J(\psi_2, \gamma_2(S_T + S_S)) + \gamma_2 J(g', h_1) - \\ &g\gamma_2 \left(J\left(\frac{h_1}{\rho_2}, \rho_1\right) + \frac{1}{2} J\left(\frac{h_2}{\rho_2}, \rho_2\right) \right). \end{aligned}$$

Assuming a small Rossby number and high correlation between densities and constant heights, we can neglect most terms:

$$\begin{aligned} \frac{Dq_1}{Dt} &= -\gamma_1^2 f(S_T + S_S), \\ \frac{Dq_2}{Dt} &= \gamma_2^2 f(S_T + S_S). \end{aligned}$$

The last terms remaining are the ones relating the exchange of vorticity due to the exchange of mass, in order to conserve the total vorticity. One could not bother and assume that the mass exchange is not done in a PV preserving kind of way and neglect them, which is the approach we will take here.

PV inversion The PV perturbations can be written as:

$$q_i \approx \frac{1}{\bar{\rho}_i H_i} \left(f + \omega_i - \frac{f}{H_i} h'_i - \frac{f}{\bar{\rho}_i} \rho'_i \right)$$

The resulting set of simplified equations is:

$$\begin{aligned} \psi_1 &= \frac{g}{f} (h'_1 + h'_2), \\ \nabla^2(\psi_2 - \psi_1) &= -\nabla \cdot \left(\frac{g'}{f} \nabla h'_1 \right), \\ q_i &= \nabla^2 \psi_i - \frac{f}{H_i} h'_i - \frac{f}{\bar{\rho}_i} \rho'_i, \\ \partial_t q_i + J(\psi_i, q_i) &= 0. \end{aligned} \tag{18}$$

Looking more closely at the inversion equations:

$$\begin{aligned} \xi_1 &= q_1 - \frac{f}{\bar{\rho}_1} \rho_1 = \nabla^2 \psi_2 - \nabla \cdot \left(\frac{g'}{f} \nabla h'_1 \right) - \frac{f}{H_1} h'_1, \\ \xi_2 &= q_2 - \frac{f}{\bar{\rho}_2} \rho_2 = \nabla^2 \psi_2 + \frac{f}{H_2} h'_1 - \frac{f^2}{g H_2} \psi_1. \end{aligned}$$

We use the rigid lid approximation to neglect the last term in ξ_2 , leading to:

$$\begin{aligned} \xi_1 &= \nabla^2 \psi_2 + \nabla \cdot \left(\frac{g'}{f} \nabla h_1 \right) - \frac{f}{H_1} h'_1, \\ \xi_2 &= \nabla^2 \psi_2 + \frac{f}{H_2} h'_1. \end{aligned} \tag{19}$$

One can solve the baroclinic equations for h_1 :

$$\xi_2 - \xi_1 = -\nabla \cdot \left(\frac{g'}{f} \nabla h'_1 \right) + \left(\frac{1}{H_1} + \frac{1}{H_2} \right) f h'_1. \tag{20}$$

with homogeneous dirichlet BCs.

Which enables to solve for ψ_i :

$$\begin{aligned} \xi_1 + \frac{f}{H_1} h'_1 &= \nabla^2 \psi_1, \\ \xi_2 - \frac{f}{H_2} h'_1 &= \nabla^2 \psi_2. \end{aligned} \tag{21}$$

This then gives us h_2 :

$$h'_2 = \frac{f}{g} \psi_1 - h'_1.$$

So this means that the system we are looking at consists of 6 advection equations, one helmholtz equation and 2 poisson's equation.

References

- [1] T. Brooke Benjamin. Gravity currents and related phenomena. *Journal of Fluid Mechanics*, 31(02):209–248, 1968.
- [2] Stern M. E. and Chassignet E. P. Mechanism of eddy separation from coastal currents. *Journal of Marine Research*, 58:269–295, 2000.
- [3] A. E. Gill. Adjustment under gravity in a rotating channel. *Journal of Fluid Mechanics*, 77(03):603–621, 1976.
- [4] Melvin E. Stern. Geostrophic fronts, bores, breaking and blocking waves. *Journal of Fluid Mechanics*, 99(04):687–703, 1980.
- [5] Melvin E. Stern, John A. Whitehead, and Bach-Lien Hua. The intrusion of a density current along the coast of a rotating fluid. *Journal of Fluid Mechanics*, 123(-1):237–265, 1983.
- [6] Marshall Ward. Experimental study of double diffusive gravity currents under rotation. In Woods Hole Oceanographic Institution, editor, *Proceedings of the GFD Program*, volume 46, 2004.